



# Estimation of surface ammonia concentrations and emissions in China from the polar-orbiting Infrared Atmospheric Sounding Interferometer and the FY-4A Geostationary Interferometric Infrared Sounder

Pu Liu<sup>1</sup>, Jia Ding<sup>1</sup>, Lei Liu<sup>1</sup>, Wen Xu<sup>2</sup>, and Xuejun Liu<sup>2</sup>

<sup>1</sup>College of Earth and Environmental Sciences, Lanzhou University, Lanzhou 730000, China

<sup>2</sup>College of Resources and Environmental Sciences, Center for Resources, Environment and Food Security, Key Laboratory of Plant-Soil Interactions, Ministry of Education, China Agricultural University, Beijing 100193, China

**Correspondence:** Lei Liu (liuleigeo@lzu.edu.cn)

Received: 28 February 2022 – Discussion started: 24 March 2022

Revised: 16 June 2022 – Accepted: 25 June 2022 – Published: 14 July 2022

**Abstract.** Ammonia (NH<sub>3</sub>) is the most important alkaline gas in the atmosphere, which has negative effects on biodiversity, ecosystems, soil acidification and human health. China has the largest NH<sub>3</sub> emissions globally, mainly associated with agricultural sources including nitrogen fertilizer and livestock. However, there is still a limited number of ground monitoring sites in China, hindering our understanding of both surface NH<sub>3</sub> concentrations and emissions. In this study, using the polar-orbiting satellite (Infrared Atmospheric Sounding Interferometer – IASI) and Fengyun-4A Geostationary Interferometric Infrared Sounder (GIIRS), we analyzed the changes in hourly NH<sub>3</sub> concentrations and estimated surface NH<sub>3</sub> concentrations and NH<sub>3</sub> emissions in China. GIIRS-derived NH<sub>3</sub> concentrations in the daytime were generally higher than those at night, with high values during 10:00–16:00 local time. Satellite-derived surface NH<sub>3</sub> concentrations were generally consistent with the ground observations, with *R*-square at 0.72 and slope equal to 1.03. Satellite-based NH<sub>3</sub> emissions ranged from 12.17 to 17.77 Tg N yr<sup>-1</sup> during 2008–2019. Spatially, high values of NH<sub>3</sub> emissions mainly occurred in the North China Plain, Northeast China and the Sichuan Basin, while low values were mainly distributed in West China (Qinghai–Tibet Plateau). Our study shows a high predictive power of using satellite data to estimate surface NH<sub>3</sub> concentrations and NH<sub>3</sub> emissions over multiple temporal and spatial scales, which provides an important reference for understanding NH<sub>3</sub> changes over China.

## 1 Introduction

Ammonia (NH<sub>3</sub>) is a highly active gas in the atmosphere and the most important alkaline gas, playing an important role in atmospheric chemistry (Fowler et al., 2013). NH<sub>3</sub> reacts with acid pollutants (SO<sub>2</sub> and NO<sub>x</sub>) to form fine particulate matter, such as PM<sub>2.5</sub>, leading to haze pollution. In addition, the deposition of NH<sub>3</sub> and NH<sub>4</sub><sup>+</sup> could also cause environmental problems such as water eutrophication, biodiversity loss and soil acidification (Paerl et al., 2014). China has become a major region for NH<sub>3</sub> emissions globally because of rapid

growth of population and agricultural production (Zhang et al., 2017; Liu et al., 2022). To provide a scientific basis for dealing with NH<sub>3</sub> pollution, it is urgent to accurately estimate both surface NH<sub>3</sub> concentrations and emissions in China.

Surface NH<sub>3</sub> concentrations can be estimated by ground measurements and model simulations. Ground measurements are considered to be the most accurate quantitative method. Current national NH<sub>3</sub> observation networks in China include the National Nitrogen Deposition Monitoring Network (NNDMN) established by China Agricultural University (Xu et al., 2015) and the Ammonia Monitoring

Network (AMoN-China) established based on the Chinese Ecosystem Research Network (CERN) (Pan et al., 2018). The NNDMN can measure ground  $\text{NH}_3$  concentrations since 2010, while AMoN-China only makes the measurements in 2015–2016. The above two monitoring networks both monitor surface  $\text{NH}_3$  concentrations on a monthly basis and lack monitoring of the hourly  $\text{NH}_3$  changes. Some studies have conducted research on the intra-day/hourly changes in  $\text{NH}_3$  concentrations based on ground observations. Werner et al. (2017) measured hourly  $\text{NH}_3$  concentration in 2012 at the Harwell site in the UK and found that high  $\text{NH}_3$  concentration usually occurred in the afternoon. Similarly, Kutzner et al. (2021) observed the hourly  $\text{NH}_3$  concentration at the SIRT Observatory in Paris and found that  $\text{NH}_3$  concentration was highest in the late afternoon. Pandolfi et al. (2012) studied the day–night cycle of  $\text{NH}_3$  concentration at the two stations in Barcelona in summer and found that the  $\text{NH}_3$  concentration was highly associated with local meteorology and traffic emissions. However, there is still a limited number of monitoring sites on the hourly  $\text{NH}_3$  changes in China.

Agricultural fertilizer and livestock production have led to a large amount of  $\text{NH}_3$  emissions. China's cultivated land area accounts for less than 10 % of the world, but it consumes about 30 % of the world's nitrogen (N) fertilizer (Peng et al., 2002). Estimation of  $\text{NH}_3$  emissions is mainly based on a bottom-up method using  $\text{NH}_3$  source statistics (fertilization, animal husbandry, etc.) and emission factors. Zhou et al. (2016) calculated the annual farmland  $\text{NH}_3$  emission ( $3.96 \pm 0.76 \text{ Tg N yr}^{-1}$ ) over China in 2008 based on the bottom-up method, which was 40 % higher than the emission in the Intergovernmental Panel on Climate Change (IPCC) Tier-1 guidelines ( $2.89 \text{ Tg N yr}^{-1}$ ). Zhang et al. (2017) reassessed China's  $\text{NH}_3$  emissions based on the mass balance method and found that  $\text{NH}_3$  emissions increased from  $12.1 \pm 0.8$  in 2000 to  $15.6 \pm 0.9 \text{ Tg N yr}^{-1}$  in 2015, with an annual growth rate of 1.9 %. Fu et al. (2020) estimated that China's  $\text{NH}_3$  emissions increased from 4.7 in 1980 to  $11 \text{ Tg N yr}^{-1}$  in 2016. Although many studies regarding  $\text{NH}_3$  emissions have been carried out in China, great uncertainties and large ranges ( $7\text{--}16 \text{ Tg N yr}^{-1}$ ) still existed in the estimates of China's  $\text{NH}_3$  emissions (Dong et al., 2010; Huang et al., 2012; Kang et al., 2016).

Besides the bottom-up estimates, some studies used data assimilation methods by ground monitoring data to constrain  $\text{NH}_3$  emission estimates. Paulot et al. (2014) assimilated GEOS-Chem with ground observations of wet reactive Nitrogen ( $N_r$ ) deposition and estimated China's  $\text{NH}_3$  emission as  $8.4 \text{ Tg N yr}^{-1}$  in 2008, with seasonal  $\text{NH}_3$  emission peaking in summer. Gilliland et al. (2003) used the data assimilation method by the Community Multiscale Air Quality (CMAQ) with the wet  $\text{NH}_4^+$  concentration data from the USA National Atmospheric Deposition Program Network and found that obvious seasonal differences appeared in  $\text{NH}_3$  emissions linked to N fertilizer and temperature. Kong et al. (2019) carried out inversion by assimilating surface AMoN  $\text{NH}_3$  ob-

servations and improved the accuracy of temporal and spatial patterns of  $\text{NH}_3$  emissions in China.

In recent years, atmospheric remote sensing has developed rapidly, which can monitor  $\text{NH}_3$  at a global scale, including the polar-orbiting satellite instruments such as the Tropospheric Emission Spectrometer (TES), Infrared Atmospheric Sounding Interferometer (IASI), Cross-track Infrared Sounder (CrIS), Atmospheric Infrared Sounder (AIRS), and Greenhouse Gases Observing Satellite (GOSAT) (Someya et al., 2020). Many studies have reported the effectiveness of using satellite data to study  $\text{NH}_3$  dynamics. Pinder et al. (2011) found that TES observation can capture spatial–temporal  $\text{NH}_3$  patterns compared with surface measurement. Van Damme et al. (2014) studied the seasonal and annual  $\text{NH}_3$  changes in the Northern Hemisphere and Southern Hemisphere using the IASI  $\text{NH}_3$  column data and found that the seasonality in the Southern Hemisphere is mainly related to biomass burning. Shephard and Cady-Pereira (2015) developed the CrIS  $\text{NH}_3$  inversion algorithms and found that CrIS can capture the global spatial distribution of  $\text{NH}_3$  concentration. Warner et al. (2016) identified the main hotspots of agricultural  $\text{NH}_3$  regions using AIRS, such as South Asia, China, the United States and some parts of Europe, and found that  $\text{NH}_3$  concentrations had increased in these agricultural regions since 2003. In addition, some studies also used the satellite measurements to improve the estimates of  $\text{NH}_3$  emissions. Zhang et al. (2017) developed a top-down inversion method using TES  $\text{NH}_3$  observation to quantify China's  $\text{NH}_3$  emission and obtained annual  $\text{NH}_3$  emission as  $11.7 \text{ Tg N yr}^{-1}$  in 2008. Marais et al. (2021) estimated  $\text{NH}_3$  emissions in the UK based on the IASI and CrIS and found that the relative errors of IASI-derived  $\text{NH}_3$  emissions were 11 %–36 % and 9 %–27 %, respectively. Van Damme et al. (2018) used the high-resolution IASI  $\text{NH}_3$  maps to identify, classify and quantify  $\text{NH}_3$  emission hotspots in the world, which was helpful for understanding the human point  $\text{NH}_3$  sources. Dammers et al. (2019) identified global 249  $\text{NH}_3$  emission point sources based on CrIS, whose total emission was about 2.5 times higher than that reported in the HTAPv2 emissions.

Besides the polar-orbiting satellite, China's Geostationary Interferometric Infrared Sounder (GIIRS) on board the Chinese FY-4A satellite can measure hourly changes in atmospheric  $\text{NH}_3$  in almost all of Asia per day, which provides great potential to study the diel cycle of  $\text{NH}_3$ . In this study, GIIRS is used to study the  $\text{NH}_3$  diel cycle (hourly changes), which is essential for understanding the differences between different times in a day by the polar-orbiting satellites (such as the IASI at 09:30 and CrIS at 13:30). Second, the surface  $\text{NH}_3$  concentration in China is estimated based on both GIIRS and IASI, which is then compared with the NNDMN. Third,  $\text{NH}_3$  emission in China is calculated based on satellite-derived surface  $\text{NH}_3$  concentration and the feedback relationship between surface  $\text{NH}_3$  concentration and emission by a chemistry transport model (GEOS-Chem). Fi-

nally, the spatial–temporal characteristics of satellite-derived surface  $\text{NH}_3$  concentration and emission are analyzed, and the uncertainties are discussed.

## 2 Data and methods

### 2.1 Satellite GIIRS $\text{NH}_3$

The Geostationary Interferometric Infrared Sounder (GIIRS) on board the Fengyun-4A geostationary satellite (FY-4A) launched by China in 2016 is the world's first hyperspectral atmospheric infrared sounder (Cai et al., 2020). The FY-4A GIIRS-detected spectral range is  $700\text{--}2250\text{ cm}^{-1}$ , including 1648 spectral channels and 14 radiation-imaging channels, covering visible light, shortwave, medium and long-wave infrared bands. The spatial resolutions of the detector are 2.0 km in the visible bands and 16 km in the infrared bands. It covers almost the whole of Asia and scans 10 times a day (Zhang et al., 2019). The GIIRS can detect the temperature and humidity profiles and trace gases at high frequencies.

$\text{NH}_3$  has two large absorption characteristics in the long-wave infrared (about  $930$  and  $965\text{ cm}^{-1}$ ). The contribution of  $\text{NH}_3$  to the brightness temperature of these two bands is between 2 and 4 K. The core of inversion algorithms is based on the so-called hyperspectral radiation index (HRI), which quantifies the spectral characteristics of  $\text{NH}_3$ . The HRI depends on whether the satellite instrument detects the presence of  $\text{NH}_3$ . The average value of the HRI is 0 with a standard deviation of 1, and the HRI range is  $[-1, 1]$ . The algorithm for estimating IASI  $\text{NH}_3$  column concentration is to convert the HRI into a column using the so-called neural network (Clarisse et al., 2021).

In this study, we use hourly  $\text{NH}_3$  concentrations during 2019–2020 (from November 2019 to October 2020) to study the  $\text{NH}_3$  diel cycle with a resolution of  $0.5^\circ$ . The original data are in Hierarchical Data Format Version 5 (HDF5), and the unit of  $\text{NH}_3$  is  $\text{molec. cm}^{-2}$ . The data are processed with MATLAB software. First, observations with considerable uncertainties (relative error exceeds 50 %) and high clouds (cloud cover exceeds 20 %) are removed (Fig. S1a in the Supplement). Secondly, the world standard time (UTC) by GIIRS is converted to local time (LT).

### 2.2 Satellite IASI $\text{NH}_3$

The IASI instrument is on board the polar solar-synchronous Metop-A platform. It has been running stably since 2006 to measure the infrared radiation emitted by the Earth (Van Damme et al., 2014). IASI can measure the infrared radiation emitted by the Earth's surface and atmosphere in the spectral range of  $645\text{--}2760\text{ cm}^{-1}$ . It can observe the world twice a day and cross the Equator at 09:30 and 21:30 local time, with a spatial resolution of 12 km at nadir. However, only daytime satellite measurements are used, because nighttime measure-

ments usually have greater uncertainties related to thermal contrasts (Van Damme et al., 2017).

The near-real-time dataset of the total  $\text{NH}_3$  column (built by artificial neural network for IASI, ANNI; ANNI- $\text{NH}_3\text{-v3}$ ) was used here. The properties of IASI  $\text{NH}_3$  data include  $\text{NH}_3$  column concentration, longitude, latitude, measurement time, cloud cover, uncertainty, solar zenith angle and other parameters. The daily  $\text{NH}_3$  column from 2008 to 2019 was used. The format of the original data is the Network Common Data Format, and the unit is  $\text{mol m}^{-2}$ . The observation data with cloud cover larger than 20 % and the uncertainty above 50 % were removed (Fig. S1b). We gridded the data to  $0.1^\circ$  by using the arithmetic average methods.

### 2.3 Ground $\text{NH}_3$ measurements

Surface  $\text{NH}_3$  concentrations in the NNDMN were used to compare with the satellite estimates including 43 observation stations. The land types of the NNDMN sites cover cities, farmland, coastal areas, forests and grasslands. Measurements during the period from January 2010 to December 2015 by the NNDMN were used. Surface  $\text{NH}_3$  concentrations were measured using an active DELTA (Denuder for Long-Term Atmospheric sampling) (Flechar et al., 2011). For the hourly measurements, we collected the data from the published papers, including five sites (Table S1 in the Supplement), Xianghe ( $39.75^\circ\text{ N}$ ,  $116.96^\circ\text{ E}$ ; December 2017–February 2018) (He et al., 2020), Fudan University ( $31.30^\circ\text{ N}$ ,  $121.50^\circ\text{ E}$ ; 1 July 2013–30 September 2014) (Wang et al., 2015), Dianshan Lake ( $31.09^\circ\text{ N}$ ,  $120.98^\circ\text{ E}$ ; 1 July 2013–30 June 2014) (Wang et al., 2015), Jinshan Chemical Industry Park ( $30.73^\circ\text{ N}$ ,  $121.27^\circ\text{ E}$ ; 6 January–30 June 2014) (Wang et al., 2015) and Gucheng ( $39.15^\circ\text{ N}$ ,  $115.73^\circ\text{ E}$ ; March 2016–May 2017) (Kuang et al., 2020). The Xianghe site in Hebei Province and the Dianshan Lake site in Shanghai represent rural environments. Jinshan Chemical Industry Park represents industrial environments. The Gucheng site in Hebei and the Fudan University site in Shanghai represent urban environments.

### 2.4 GEOS-Chem

The GEOS-Chem model version 12.3.0 is a three-dimensional chemistry transport model developed by Harvard University, which has been widely used in the field of atmospheric studies (Eastham et al., 2014). The nested regional model in Asia was used in this study driven by assimilated GEOS-5 meteorological data at a horizontal resolution of  $1/2^\circ \times 2/3^\circ$ . Dry deposition calculation in GEOS-Chem follows a standard resistance-in-series model (Wesely, 2007), while wet deposition includes both convective updraft and large-scale precipitation scavenging (Jacob, 1999). The GEOS-Chem model here does not consider land–atmosphere bidirectional  $\text{NH}_3$  exchange, and the  $\text{NH}_3$  flux was parameterized as uncoupled emission and dry deposition processes.

Anthropogenic emissions over China were from the Regional Emission in Asia (REAS-v2) inventory. The GEOS-Chem outputs of NH<sub>3</sub> concentrations include 47 layers from the ground to the top of the atmosphere, which were used to capture NH<sub>3</sub> vertical profiles. The feedback between surface NH<sub>3</sub> concentration and emissions was also calculated by GEOS-Chem.

## 2.5 Satellite-based surface NH<sub>3</sub> estimates and emissions

Surface NH<sub>3</sub> concentrations were estimated using the satellite NH<sub>3</sub> columns as well as NH<sub>3</sub> vertical profiles. To gain the continuous vertical NH<sub>3</sub> profile, the Gaussian function was used to fit the 47 layers' NH<sub>3</sub> concentrations. A three-parameter Gaussian function was used to fit NH<sub>3</sub> vertical profiles at each grid box from GEOS-Chem according to previous studies (Liu et al., 2019).

$$\rho(Z) = \sum_{i=1}^n \rho_{\max,i} e^{-\left(\frac{Z-Z_{0,i}}{\sigma_i}\right)^2}, \quad (1)$$

where  $Z$  is the height of a layer in an atmospheric chemical transport model (ACTM);  $\rho_{\max}$ ,  $Z_0$  and  $\sigma$  are the maximum of NH<sub>3</sub> concentration, the corresponding height with the maximum of NH<sub>3</sub> concentration and the thickness of the NH<sub>3</sub> concentration layer (1 standard error of the Gaussian function).

The satellite-derived NH<sub>3</sub> concentration at the height of  $h_G$  can be calculated as

$$S_{G_{\text{NH}_3}} = S_{\text{trop}} \times \frac{\rho(h_G)}{\int_0^{h_{\text{trop}}} \rho(Z) dx} \times \frac{G_{\text{ACTM}}^{1-24}}{G_{\text{ACTM}}^{\text{overpass}}}, \quad (2)$$

where  $\frac{\rho(h_G)}{\int_0^{h_{\text{trop}}} \rho(Z) dx}$  represents the ratio of NH<sub>3</sub> concentration at the height of  $h_G$  to total columns ( $\int_0^{h_{\text{trop}}} \rho(Z) dx$ ),  $S_{\text{trop}}$  represents satellite-derived NH<sub>3</sub> columns, and  $\frac{G_{\text{ACTM}}^{1-24}}{G_{\text{ACTM}}^{\text{overpass}}}$  is the ratio of average surface NH<sub>3</sub> concentration ( $G_{\text{ACTM}}^{1-24}$ ) to that at satellite overpass time ( $G_{\text{ACTM}}^{\text{overpass}}$ ) by an ACTM.

The mass balance method (Lamsal et al., 2011; Geddes and Martin, 2017; Cooper et al., 2017) was used to exploit the feedback ratio of surface NH<sub>3</sub> concentrations and NH<sub>3</sub> emissions (Marais et al., 2021):

$$E_s = S_{G_{\text{NH}_3}} \times \left( \frac{E}{G_{G_{\text{NH}_3}}} \right)_m, \quad (3)$$

where  $E_s$  is satellite-based NH<sub>3</sub> emissions,  $S_{G_{\text{NH}_3}}$  is satellite-derived surface NH<sub>3</sub> concentrations and  $\left( \frac{E}{G_{G_{\text{NH}_3}}} \right)_m$  is the ratio of surface NH<sub>3</sub> concentrations and NH<sub>3</sub> emissions simulated by GEOS-Chem.

## 3 Results and discussions

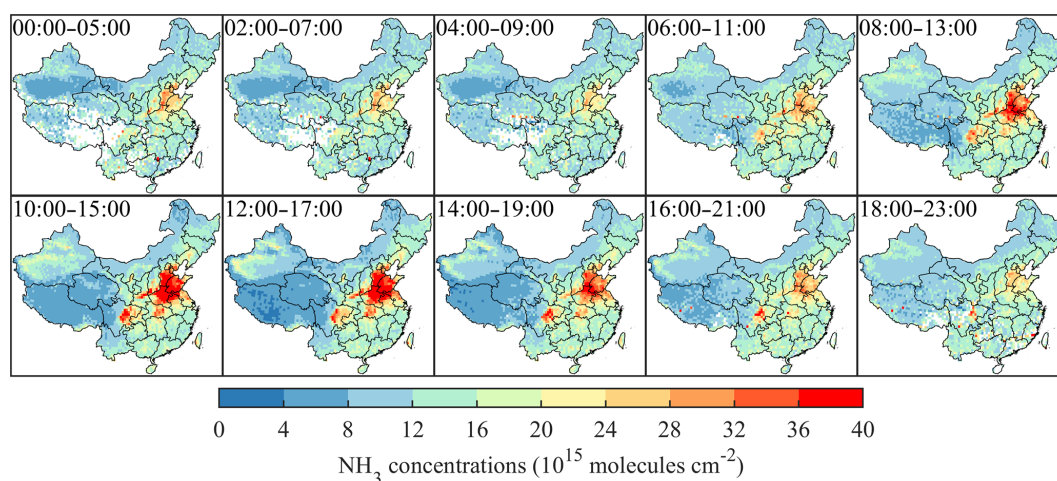
### 3.1 GIIRS-based hourly NH<sub>3</sub> concentrations during 2019–2020

Figure 1 shows the hourly NH<sub>3</sub> concentrations observed from GIIRS during 2019–2020. Daytime NH<sub>3</sub> columns were significantly higher than those at night. The intra-day hourly NH<sub>3</sub> columns showed an overall increase first and then a decrease, with high values during 10:00–16:00. The increase in temperature enhanced the volatilization of NH<sub>3</sub>, which may explain high values of NH<sub>3</sub> concentrations during the daytime.

Ground-based measurements of hourly NH<sub>3</sub> concentrations are very lacking, and the timespan may be different from GIIRS measurements. Here we only used them to show the hourly patterns of NH<sub>3</sub> concentrations (Fig. 2). The Xiangehe site in Hebei Province and Dianshan Lake site in Shanghai represent rural environments. Jinshan Chemical Industry Park represents industrial environments. The Gucheng site in Hebei and the Fudan University site in Shanghai represent urban environments.

NH<sub>3</sub> concentration in the rural environment basically shows a normal distribution, and high NH<sub>3</sub> concentration generally appears between 09:00 and 16:00, which may be related to agricultural activities and temperature. In the industrial environment (Jinshan Chemical Industry Park, JSP), NH<sub>3</sub> concentration fluctuates irregularly, and two peaks appear at 18:00–23:00 and 06:00–08:00, while NH<sub>3</sub> concentration tends to be stable at other times. In the urban environment, the changes in NH<sub>3</sub> concentration by satellite at the Gucheng site are consistent with ground monitoring, showing a clear peak around 09:00–14:00. NH<sub>3</sub> concentration at the Fudan University site gradually decreases from the morning peak to the afternoon. The evaporation of dew may drive the NH<sub>3</sub> increase from the morning to the noon (Wang et al., 2015). NH<sub>3</sub> concentration by ground monitoring in cities (Gucheng and Fudan University) has double peaks between 08:00–11:00 and 18:00–22:00, which may also be related to traffic emissions. In summary, except for industrial sites, hourly NH<sub>3</sub> in China has a large variability between day and night, and the hourly NH<sub>3</sub> patterns are affected by many factors, of which anthropogenic emissions and temperature seem to be the most important drivers.

Spatial distribution of GIIRS-based surface NH<sub>3</sub> concentrations across China had large variability (Fig. 3). High surface NH<sub>3</sub> concentration ( $> 10 \mu\text{g N m}^{-3}$ ) is mainly concentrated in the North China Plain (NCP), followed by the Sichuan Basin, Northeast China and parts of Xinjiang, while low values ( $< 4 \mu\text{g N m}^{-3}$ ) are mainly concentrated in the Qinghai–Tibet Plateau. High surface NH<sub>3</sub> concentration ( $126.85 \mu\text{g N m}^{-3}$ ) appears in July ( $6.78 \mu\text{g N m}^{-3}$  on average), and the lowest value ( $0.23 \mu\text{g N m}^{-3}$ ) appears in November ( $3.25 \mu\text{g N m}^{-3}$  on average). There are obvious seasonal changes in surface NH<sub>3</sub> concentrations in the NCP



**Figure 1.** Monthly average  $\text{NH}_3$  concentrations for each of the 10 GIIRS overpass time periods during 2019–2020.

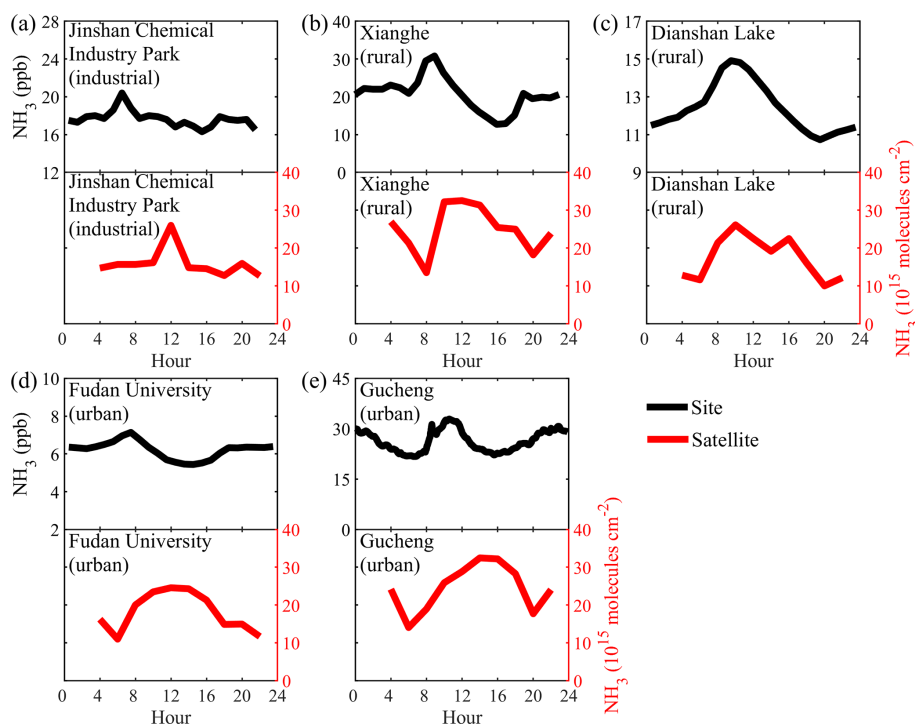


**Figure 2.** GIIRS-based and measured hourly  $\text{NH}_3$  concentrations at five sites: Jinshan Chemical Industry Park (JSP, **a**), Xianghe (XH, **b**), Dianshan Lake (DSL, **c**), Fudan University (FDU, **d**) and Gucheng (GC, **e**).

with high values in summer and low values in winter, related to both agricultural N fertilizer and higher temperature.

### 3.2 IASI-based $\text{NH}_3$ surface concentrations

The observation data of the NNDMN in China were collected to compare with the IASI-derived surface  $\text{NH}_3$  concentration. In general, a good consistency was found between measurements and satellite estimates, with the regression  $R^2$  as

0.72 and the RMSE as  $2.24 \mu\text{g N m}^{-3}$ . The coefficient of the fitted line was  $1.03 \approx 1$ , and the bias was 2.59 % (Fig. 4).

Monthly regression  $R^2$  between the satellite-derived  $\text{NH}_3$  concentration and the measured  $\text{NH}_3$  was 0.38–0.84 (Fig. 5). The regression  $R^2$  reached the higher value ( $> 0.80$ ) in July and August. The RMSE ranged from 2.29 to  $3.36 \mu\text{g N m}^{-3}$ , which reached the maximum value of  $3.36 \mu\text{g N m}^{-3}$  in July and reached the smallest value in March ( $2.29 \mu\text{g N m}^{-3}$ ). The bias is basically less than 31 % for all months and reached the minimum value of 0.67 % in February, indicat-

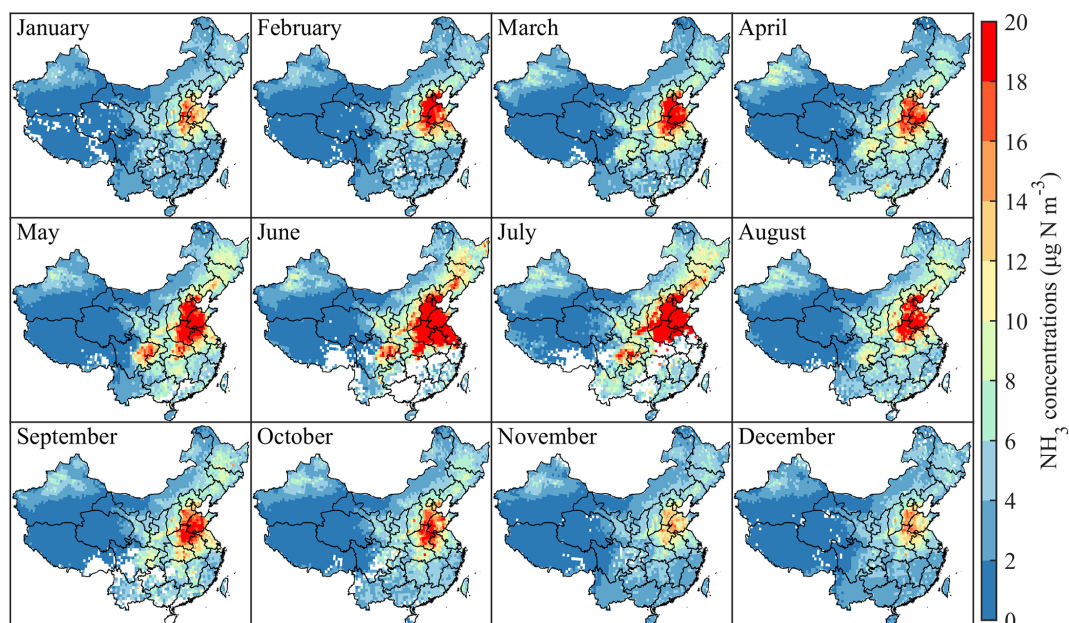


**Figure 3.** Spatial distribution of monthly surface  $\text{NH}_3$  concentrations in China by GIIRS in 2019–2020.

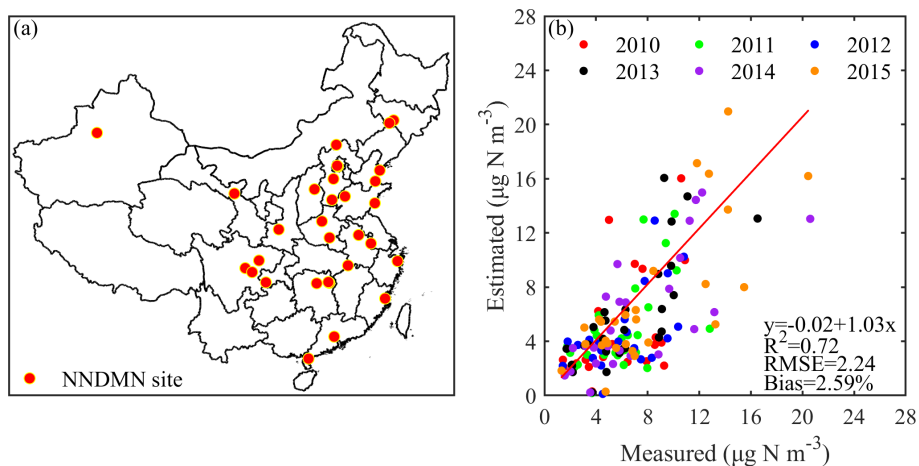


**Figure 4.** Comparison of IASI surface  $\text{NH}_3$  concentrations with NNDMN measurements. (a) The locations of NNDMN; (b) the regression results between satellite estimates and measurements.

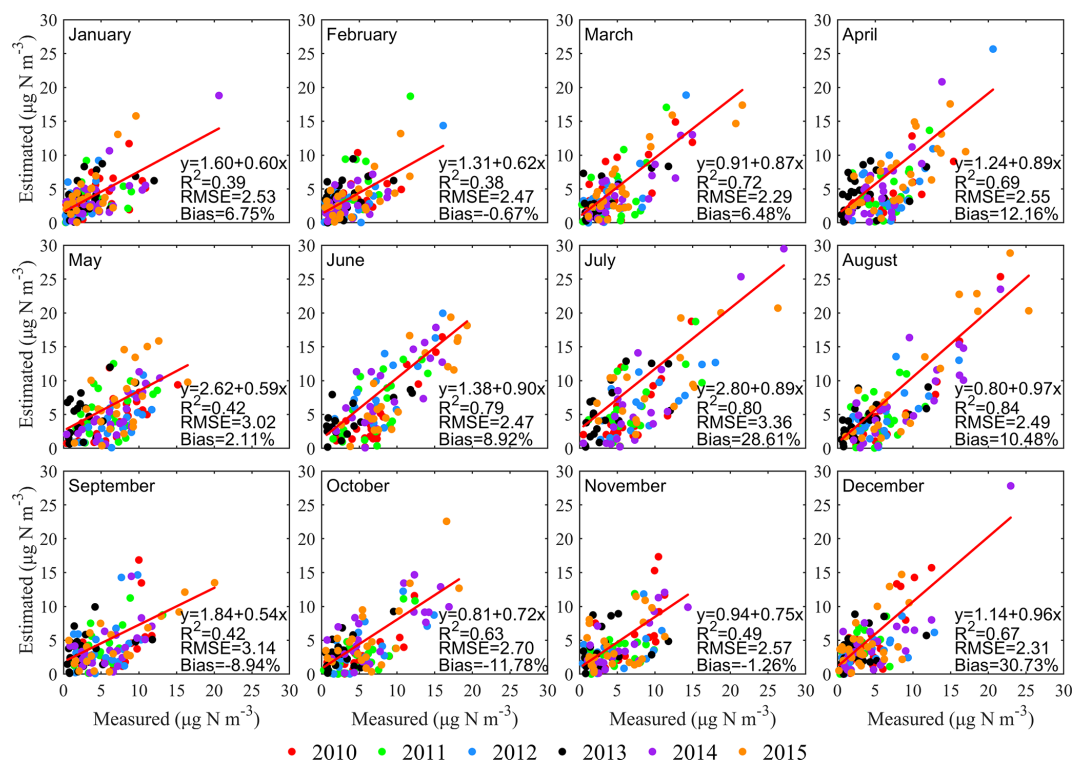
ing that the monthly IASI-derived surface concentrations obtained are consistent with measurements.

Figure 6 shows the monthly changes in surface  $\text{NH}_3$  concentrations in Huinong County in Ningxia from 2010 to 2015 for a total of 72 months. Surface  $\text{NH}_3$  concentrations retrieved by the IASI were compared with the observation data at Huinong. The highest value of each year basically appeared from June to August, and the lowest values appeared from December to January. In the past 6 years, the maximum measured  $\text{NH}_3$  concentration appeared in June 2015 ( $18.9 \mu\text{g N m}^{-3}$ ), and the minimum appeared in November 2012 ( $0.6 \mu\text{g N m}^{-3}$ ). The observation data and satellite data have the same seasonal changes.

Figures 3 and 7 show the spatial distribution of GIIRS-derived and IASI-derived surface  $\text{NH}_3$  concentrations in 2019. The spatial distribution and gradients of surface  $\text{NH}_3$  concentrations by the GIIRS and IASI have the same gradients from the eastern to western regions. One notable difference occurred in the middle and lower reaches of the Yangtze River in June and July since the GIIRS observations are affected by clouds and had missing data.

### 3.3 IASI-derived $\text{NH}_3$ emissions

Based on the top-down estimates, China's  $\text{NH}_3$  emissions ranged from 12.17 to  $17.77 \text{ Tg N yr}^{-1}$  during 2008–2019.



**Figure 5.** Comparison of monthly average values of ground measured and IASI-derived NH<sub>3</sub> surface concentrations in 2010–2015.

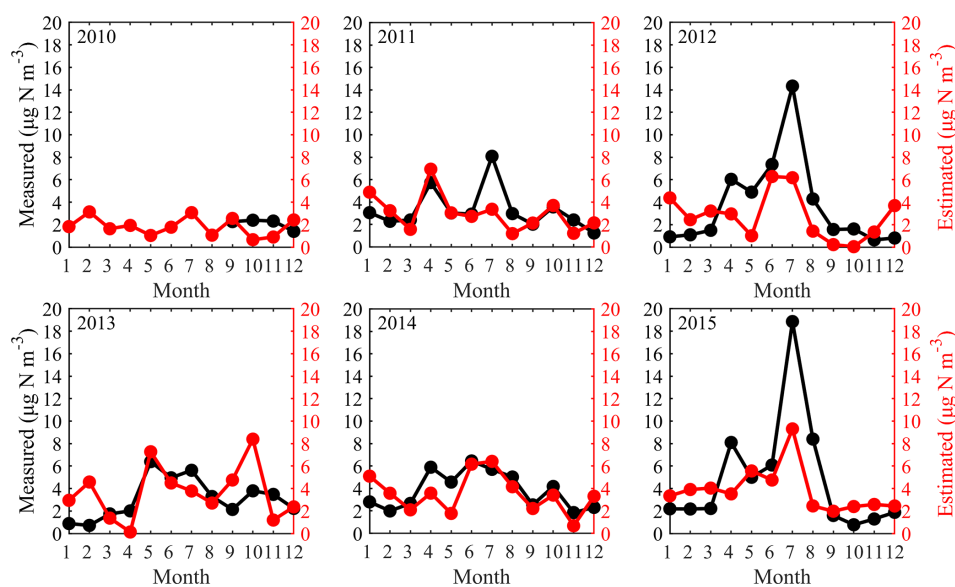


**Figure 6.** Monthly changes in NH<sub>3</sub> concentrations in Huinong County in Ningxia from 2010 to 2015 for a total of 72 months during 2010–2015.

From 2008 to 2015, NH<sub>3</sub> emissions increased from 13.00 to 17.06 Tg N yr<sup>-1</sup>. Since 2008, the temperature in China has risen steadily (Ding et al., 2007), promoting the volatilization of NH<sub>3</sub>, which partly explains the increase in NH<sub>3</sub> emissions from 2008 to 2015. After 2015, NH<sub>3</sub> emissions fluctuated and changed slightly (16.08–17.77 Tg N yr<sup>-1</sup>). Com-

pared with other studies, the change in NH<sub>3</sub> emissions from 2008 to 2015 is consistent with previous estimates, and the overall NH<sub>3</sub> emissions show an upward trend (Kang et al., 2016; Zhang et al., 2018; Ma, 2020; Fu et al., 2020; Zhang et al., 2021). Our estimates are on the rise as a whole, but the calculated values are generally lower than those by Zhang

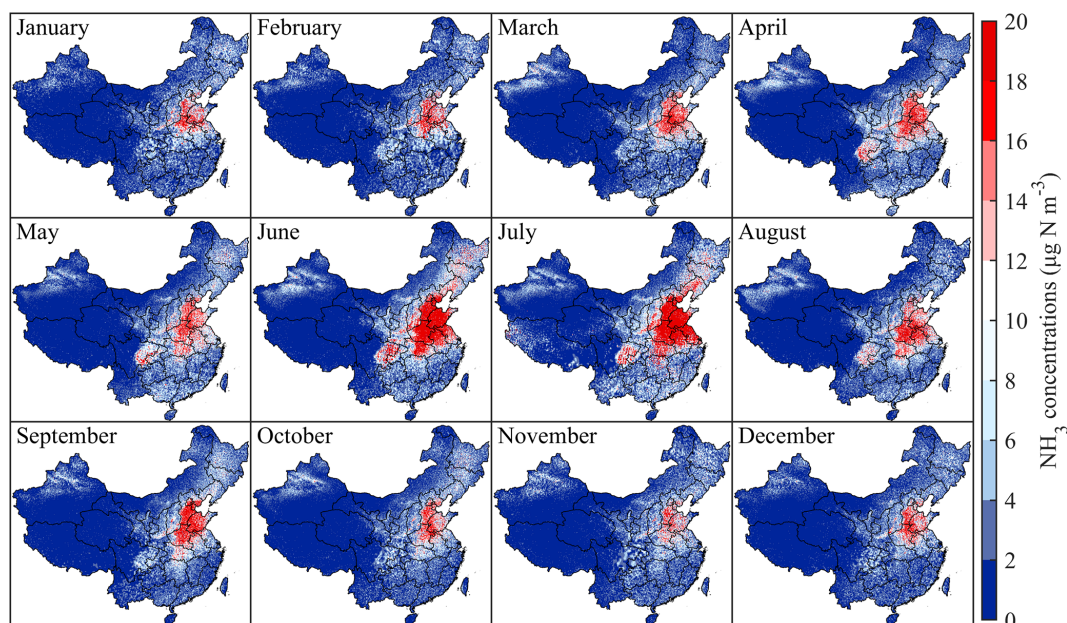


**Figure 7.** Spatial distribution of monthly surface  $\text{NH}_3$  concentrations in China by the IASI in 2019.

et al. (2017) (around  $15 \text{ Tg N yr}^{-1}$ ) but larger than those by EDGAR and Kang et al. (2016).

In terms of spatial distribution, high  $\text{NH}_3$  emissions are generally distributed in the North China Plain, Sichuan Basin and Northeast China, while the low values are mainly distributed in Southwest China (especially the Qinghai–Tibet Plateau). The North China Plain is China’s granary, with developed agriculture and animal husbandry, high population densities and strong human activities (including vehicle emissions) (Zhang et al., 2006; Wang et al., 2020). In contrast, South China is rich in rainfall, which promotes the deposition of  $\text{NH}_3$  and suppresses its volatilization to a certain extent.

The spatial distributions of  $\text{NH}_3$  emissions in January, April, July and October were selected to characterize the seasonal variations. The average emissions for the four months were  $1.15$ ,  $1.31$ ,  $2.31$  and  $1.16 \text{ kg N ha}^{-1}$  in January, April, July and October, indicating that  $\text{NH}_3$  emission is highest in summer and lowest in winter. The annual average emission intensity of 2019 is  $16.53 \text{ kg N ha}^{-1}$  ( $0.09$ – $313.47 \text{ kg N ha}^{-1}$ ). Figure 8b shows the monthly changes in  $\text{NH}_3$  emissions, which basically shows a normal distribution. High values are generally distributed in June and July, and low values are generally distributed in November and December. They reached the maximum monthly emission of  $2.6 \text{ Tg N m}^{-1}$  in July 2019 and reached the minimum monthly emission in November and December ( $1.1 \text{ Tg N m}^{-1}$ ).

#### 4 Limitations and outlook

This study developed satellite-based surface  $\text{NH}_3$  concentrations and emissions in China based on remote sensing data (IASI and GIIRS). However, several limitations have been identified in this study. First, the Fengyun geostationary satellite used in this study can achieve hourly  $\text{NH}_3$  concentrations, but the time series is still very short (November 2019–October 2020), and satellite observations are affected by clouds and meteorological conditions, resulting in missing values in parts of the Yangtze River basin.

Second, we used a relatively fixed average conversion ratio (Fig. S2) to estimate surface  $\text{NH}_3$  concentrations and  $\text{NH}_3$  emissions in China, ignoring the time-series variation of the ratio, due to the temporal constraint of the emission inventory. In this case, non-emission factors led to a higher satellite-observed  $\text{NH}_3$  column; for example, emission reductions of  $\text{SO}_2$  and  $\text{NO}_2$  led to an increased  $\text{NH}_3$  column (Lachatre et al., 2019; Fu et al., 2020), which can introduce uncertainty into  $\text{NH}_3$  emission calculations using concentration as the main parameter.

Third, the spatial resolution of the  $\text{NH}_3$  vertical profile simulated by the atmospheric model is relatively coarse ( $0.5^\circ$ ). In order to make it consistent with the spatial resolution of the remote sensing data, the outputs of GEOS-Chem (vertical profiles and feedback ratio between emissions and surface  $\text{NH}_3$  concentrations) were adjusted through resampling methods. Owing to the resolution limit, the ratio-based mass balance approach to estimate  $\text{NH}_3$  emissions neglected the effects of internal transport of  $\text{NH}_3$  and displacement of emission sources within the fine grid.

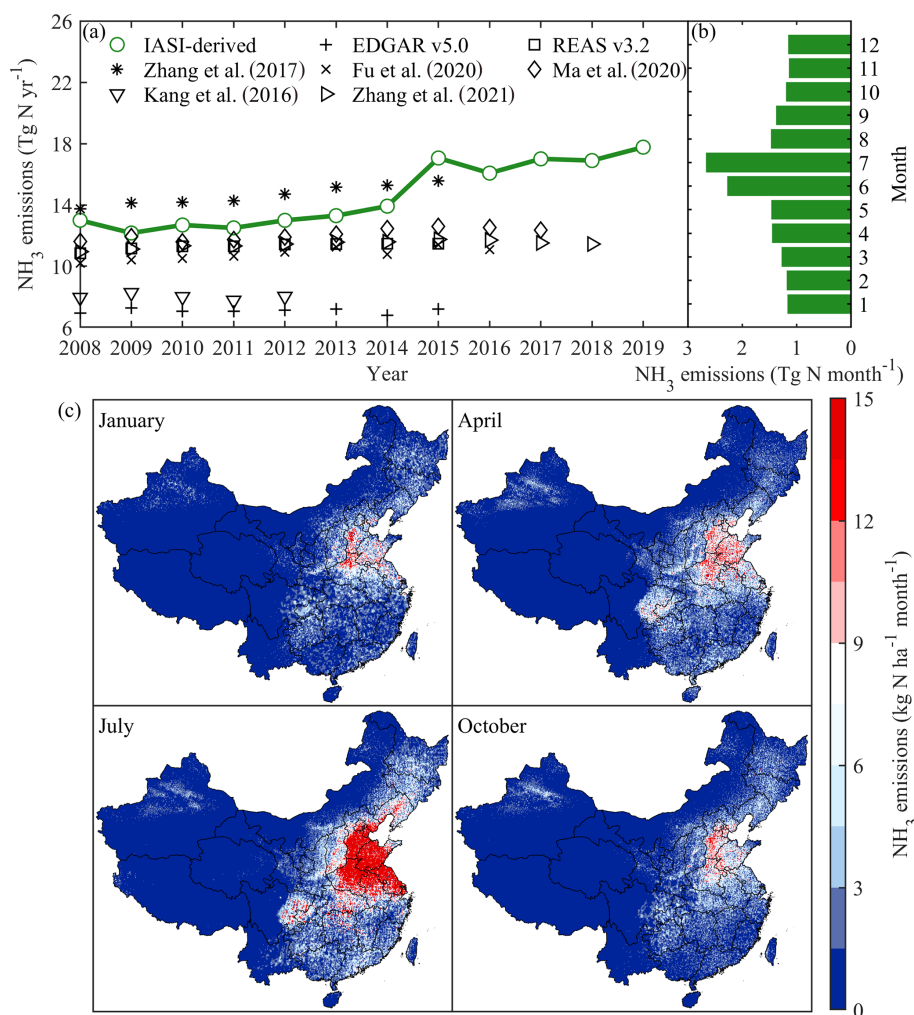


**Figure 8.** Annual changes in NH<sub>3</sub> emissions (a), monthly changes in NH<sub>3</sub> emissions in 2019 (b) and spatial distribution of NH<sub>3</sub> emissions by month in 2019 (c).

Finally, there are some uncertainties and biases in the observed NH<sub>3</sub> column by satellite. Earlier versions of the IASI NH<sub>3</sub> column product were 25 %–50 % lower than ground-based measurements (Whitburn et al., 2016; Damers et al., 2017). However, version 3 of IASI–NH<sub>3</sub> lacks a comprehensive ground-based measurement assessment, which has only been compared with limited aircraft observations (Guo et al., 2021). Comparing IASI-derived surface NH<sub>3</sub> concentrations with measurements of ground sites (NNDMN) generally shows consistency in this study. Further work is needed for the complete assessment and error analysis.

At present, there are more and more satellite sensors (GOSAT, CrIS, AIRS, etc.) that can monitor NH<sub>3</sub> concentrations. This study only used IASI and GIIRS, and in the future, data from different satellites can be merged to analyze NH<sub>3</sub> changes on multiple temporal and spatial scales.

## 5 Conclusion

We use GIIRS to study the NH<sub>3</sub> diel cycle and estimate surface NH<sub>3</sub> concentrations and emissions based on the IASI in China. There are obvious hourly changes in NH<sub>3</sub> concentration in China using GIIRS. Overall, NH<sub>3</sub> concentrations are larger in the daytime than at nighttime in China. Hourly NH<sub>3</sub> concentrations at different regions show different patterns, but high values generally appear at 10:00–16:00. Comparing ground measured and IASI-derived NH<sub>3</sub> surface concentrations by NNDMN from 2010 to 2015, the coefficient of the fitted line is  $1.03 \approx 1$  and the low bias is 2.59 %, indicating satellite estimates have good consistency with the measurements. IASI-derived Chinese NH<sub>3</sub> emissions range from 12.17 to 17.77 Tg N yr<sup>-1</sup> during 2008–2019, among which NH<sub>3</sub> emissions increase from 2008 to 2015. The emission intensity of NH<sub>3</sub> in China presents a strong spatial heterogeneity, being high in the east and low in the west. The high val-

ues are mainly distributed in the North China Plain, Sichuan Basin and Northeast China. High values are generally distributed in summer, and low values generally occur in winter. This study provides an important reference basis for the formulation of NH<sub>3</sub> pollution prevention and control policy in China.

**Data availability.** IASI NH<sub>3</sub> data were obtained from [https://iasi.aeris-data.fr/nh3\\_iasi\\_a\\_data](https://iasi.aeris-data.fr/nh3_iasi_a_data) (Clarisse et al., 2022). GIIRS NH<sub>3</sub> data were obtained from <https://doi.org/10.5281/zenodo.5051433> (Clarisse, 2021).

**Supplement.** The supplement related to this article is available online at: <https://doi.org/10.5194/acp-22-9099-2022-supplement>.

**Author contributions.** The study was conceived by LL, and data analysis was performed by JD. The paper was written by PL, with editing from WX and XL. LL was involved in obtaining the project grant and supervised the study.

**Competing interests.** The contact author has declared that none of the authors has any competing interests.

**Disclaimer.** Publisher's note: Copernicus Publications remains neutral with regard to jurisdictional claims in published maps and institutional affiliations.

**Acknowledgements.** The analysis in this study is supported by the Supercomputing Center of Lanzhou University.

**Financial support.** This study is supported by the National Natural Science Foundation of China (grant nos. 42001347, 41705130 and 41922037) and the Chinese State Key Research and Development Programme (grant nos. 2017YFC0210100 and 2017YFD0200101).

**Review statement.** This paper was edited by Theodora Nah and reviewed by three anonymous referees.

## References

Cai, X., Bao, Y., Petropoulos, G. P., Lu, F., Lu, Q., Zhu, L., and Wu, Y.: Temperature and humidity profile retrieval from FY4-GIIRS hyperspectral data using artificial neural networks, *Remote Sens.*, 12, 1872, <https://doi.org/10.3390/rs12111872>, 2020.

Clarisse, L.: Atmospheric Ammonia (NH<sub>3</sub>) total columns from the FY-4A Geostationary Interferometric Infrared Sounder (GIIRS) (Version 2), Zenodo [data set], <https://doi.org/10.5281/zenodo.5051433>, 2021.

Clarisse, L., Van Damme, M., Hurtmans, D., Franco, B., Clerbaux, C., and Coheur, P. F.: The diel cycle of NH<sub>3</sub> observed from the FY-4A Geostationary Interferometric Infrared Sounder (GIIRS), *Geophys. Res. Lett.*, 48, e2021GL093010, <https://doi.org/10.1029/2021GL093010>, 2021.

Clarisse, L., Van Damme, M., and Coheur, P.-F.: Near-real time daily IASI/Metop-A ULB-LATMOS ammonia (NH<sub>3</sub>) L2 product (total column), AERIS data infrastructure [data set], [https://iasi.aeris-data.fr/nh3\\_iasi\\_a\\_data](https://iasi.aeris-data.fr/nh3_iasi_a_data), last access: 5 February 2022.

Cooper, M., Martin, R. V., Padmanabhan, A., and Henze, D. K.: Comparing mass balance and adjoint methods for inverse modeling of nitrogen dioxide columns for global nitrogen oxide emissions, *J. Geophys. Res.-Atmos.*, 122, 4718–4734, <https://doi.org/10.1002/2016JD025985>, 2017.

Dammers, E., Shephard, M. W., Palm, M., Cady-Pereira, K., Capps, S., Lutsch, E., Strong, K., Hannigan, J. W., Ortega, I., Toon, G. C., Stremme, W., Grutter, M., Jones, N., Smale, D., Siemons, J., Hrpcek, K., Tremblay, D., Schaap, M., Notholt, J., and Erisman, J. W.: Validation of the CrIS fast physical NH<sub>3</sub> retrieval with ground-based FTIR, *Atmos. Meas. Tech.*, 10, 2645–2667, <https://doi.org/10.5194/amt-10-2645-2017>, 2017.

Dammers, E., McLinden, C. A., Griffin, D., Shephard, M. W., Van Der Graaf, S., Lutsch, E., Schaap, M., Gainairu-Matz, Y., Fioletov, V., Van Damme, M., Whitburn, S., Clarisse, L., Cady-Pereira, K., Clerbaux, C., Coheur, P. F., and Erisman, J. W.: NH<sub>3</sub> emissions from large point sources derived from CrIS and IASI satellite observations, *Atmos. Chem. Phys.*, 19, 12261–12293, <https://doi.org/10.5194/acp-19-12261-2019>, 2019.

Ding, Y. H., Ren, G. Y., Zhao, Z. C., Xu, Y., Luo, Y., Li, Q. P., and Zhang, J.: Detection, causes and projection of climate change over China: An overview of recent progress, *Adv. Atmos. Sci.*, 24, 954–971, <https://doi.org/10.1007/s00376-007-0954-4>, 2007.

Dong, W., Xing, J., and Wang, S.: Temporal and spatial distribution of anthropogenic ammonia emissions in China: 1994–2006, *Huanjing Kexue*, 31, 1457–1463, 2010.

Eastham, S. D., Weisenstein, D. K., and Barrett, S. R.: Development and evaluation of the unified tropospheric–stratospheric chemistry extension (UCX) for the global chemistry-transport model GEOS-Chem, *Atmos. Environ.*, 89, 52–63, <https://doi.org/10.1016/j.atmosenv.2014.02.001>, 2014.

Flechar, C. R., Nemitz, E., Smith, R. I., Fowler, D., Vermeulen, A. T., Bleeker, A., Erisman, J. W., Simpson, D., Zhang, L., Tang, Y. S., and Sutton, M. A.: Dry deposition of reactive nitrogen to European ecosystems: a comparison of inferential models across the NitroEurope network, *Atmos. Chem. Phys.*, 11, 2703–2728, <https://doi.org/10.5194/acp-11-2703-2011>, 2011.

Fowler, D., Coyle, M., Skiba, U., Sutton, M. A., Cape, J. N., Reis, S., Sheppard, L. J., Jenkins, A., Grizzetti, B., Galloway, J. N., Vitousek, P., Leach, A., Bouwman, A. F., Butterbach-Bahl, K., Dentener, F., Stevenson, D., Amann, M., and Voss, M.: The global nitrogen cycle in the twenty-first century, *Philos. T. R. Soc. B*, 368, 20130164, <https://doi.org/10.1098/rstb.2013.0164>, 2013.

Fu, H., Luo, Z., and Hu, S.: A temporal-spatial analysis and future trends of ammonia emissions in China, *Sci. Total Environ.*, 731, 138897, <https://doi.org/10.1016/j.scitotenv.2020.138897>, 2020.

Geddes, J. A. and Martin, R. V.: Global deposition of total reactive nitrogen oxides from 1996 to 2014 constrained with satellite

- observations of NO<sub>2</sub> columns, *Atmos. Chem. Phys.*, 17, 10071–10091, <https://doi.org/10.5194/acp-17-10071-2017>, 2017.
- Gilliland, A. B., Dennis, R. L., Roselle, S. J., and Pierce, T. E.: Seasonal NH<sub>3</sub> emission estimates for the eastern United States based on ammonium wet concentrations and an inverse modeling method, *J. Geophys. Res.-Atmos.*, 108, 4477, <https://doi.org/10.1029/2002jd003063>, 2003.
- Guo, X., Wang, R., Pan, D., Zondlo, M. A., Clarisse, L., Van Damme, M., Whitburn, S., Coheur, P. F., Clerbaux, C., Franco, B., Golston, L. M., Wendt, L., Sun, K., Tao, L., Miller, D., Mikoviny, T., Müller, M., Wisthaler, A., Tevlin, A. G., Murphy, J. G., Nowak, J. B., Roscioli, J. R., Volkamer, R., Kille, N., Neuman, J. A., Eilerman, S. J., Crawford, J. H., Yacovitch, T. I., Barrick, J. D., and Scarino, A. J.: Validation of IASI satellite ammonia observations at the pixel scale using in situ vertical profiles, *J. Geophys. Res.-Atmos.*, 126, e2020JD033475, <https://doi.org/10.1029/2020jd033475>, 2021.
- He, Y., Pan, Y., Zhang, G., Ji, D., Tian, S., Xu, X., Zhang, R., and Wang, Y.: Tracking ammonia morning peak, sources and transport with 1Hz measurements at a rural site in North China Plain, *Atmos. Environ.*, 235, 117630, <https://doi.org/10.1016/j.atmosenv.2020.117630>, 2020.
- Huang, X., Song, Y., Li, M., Li, J., Huo, Q., Cai, X., Zhu, T., Hu, M., and Zhang, H.: A high-resolution ammonia emission inventory in China, *Global Biogeochem. Cy.*, 26, GB1030, <https://doi.org/10.1029/2011gb004161>, 2012.
- Jacob, D. J.: Introduction to atmospheric chemistry, Princeton University Press, <https://doi.org/10.1515/9781400841547>, 1999.
- Kang, Y., Liu, M., Song, Y., Huang, X., Yao, H., Cai, X., Zhang, H., Kang, L., Liu, X., Yan, X., He, H., Zhang, Q., Shao, M., and Zhu, T.: High-resolution ammonia emissions inventories in China from 1980 to 2012, *Atmos. Chem. Phys.*, 16, 2043–2058, <https://doi.org/10.5194/acp-16-2043-2016>, 2016.
- Kong, L., Tang, X., Zhu, J., Wang, Z., Pan, Y., Wu, H., Wu, L., Wu, Q., He, Y., Tian, S., Xie, Y., Liu, Z., Sui, W., Han, L., and Carmichael, G.: Improved inversion of monthly ammonia emissions in China based on the Chinese ammonia monitoring network and ensemble Kalman filter, *Environ. Sci. Technol.*, 53, 12529–12538, <https://doi.org/10.1021/acs.est.9b02701>, 2019.
- Kuang, Y., Xu, W., Lin, W., Meng, Z., Zhao, H., Ren, S., Zhang, G., Liang, L., and Xu, X.: Explosive morning growth phenomena of NH<sub>3</sub> on the North China Plain: Causes and potential impacts on aerosol formation, *Environ. Pollut.*, 257, 113621, <https://doi.org/10.1016/j.envpol.2019.113621>, 2020.
- Kutzner, R. D., Cuesta, J., Chelin, P., Petit, J.-E., Ray, M., Landsheere, X., Tournadre, B., Dupont, J.-C., Rosso, A., Hase, F., Orphal, J., and Beekmann, M.: Diurnal evolution of total column and surface atmospheric ammonia in the megacity of Paris, France, during an intense springtime pollution episode, *Atmos. Chem. Phys.*, 21, 12091–12111, <https://doi.org/10.5194/acp-21-12091-2021>, 2021.
- Lachatre, M., Fortems-Cheiney, A., Foret, G., Siour, G., Dufour, G., Clarisse, L., Clerbaux, C., Coheur, P.-F., Van Damme, M., and Beekmann, M.: The unintended consequence of SO<sub>2</sub> and NO<sub>2</sub> regulations over China: increase of ammonia levels and impact on PM<sub>2.5</sub> concentrations, *Atmos. Chem. Phys.*, 19, 6701–6716, <https://doi.org/10.5194/acp-19-6701-2019>, 2019.
- Lamsal, L., Martin, R., Padmanabhan, A., Van Donkelaar, A., Zhang, Q., Sioris, C., Chance, K., Kurosu, T., and Newchurch, M.: Application of satellite observations for timely updates to global anthropogenic NO<sub>x</sub> emission inventories, *Geophys. Res. Lett.*, 38, L05810, <https://doi.org/10.1029/2010GL046476>, 2011.
- Liu, L., Zhang, X., Wong, A. Y. H., Xu, W., Liu, X., Li, Y., Mi, H., Lu, X., Zhao, L., Wang, Z., Wu, X., and Wei, J.: Estimating global surface ammonia concentrations inferred from satellite retrievals, *Atmos. Chem. Phys.*, 19, 12051–12066, <https://doi.org/10.5194/acp-19-12051-2019>, 2019.
- Liu, L., Xu, W., Lu, X., Zhong, B., Guo, Y., Lu, X., Zhao, Y., He, W., Wang, S., Zhang, X., Liu, X., and Vitousek, P.: Exploring global changes in agricultural ammonia emissions and their contribution to nitrogen deposition since 1980, *P. Natl. Acad. Sci. USA*, 119, e2121998119, <https://doi.org/10.1073/pnas.2121998119>, 2022.
- Ma, S.: High-resolution assessment of ammonia emissions in China: Inventories, driving forces and mitigation, *Atmos. Environ.*, 229, 117458, <https://doi.org/10.1016/j.atmosenv.2020.117458>, 2020.
- Marais, E. A., Pandey, A. K., Van Damme, M., Clarisse, L., Coheur, P. F., Shephard, M. W., Cady-Pereira, K. E., Misselbrook, T., Zhu, L., Luo, G., and Yu, F.: UK Ammonia Emissions Estimated With Satellite Observations and GEOS-Chem, *J. Geophys. Res.-Atmos.*, 126, e2021JD035237, <https://doi.org/10.1029/2021JD035237>, 2021.
- Paerl, H. W., Gardner, W. S., McCarthy, M. J., Peierls, B. L., and Wilhelm, S. W.: Algal blooms: noteworthy nitrogen, *Science*, 346, 175–175, <https://doi.org/10.1126/science.346.6206.175-a>, 2014.
- Pan, Y., Tian, S., Zhao, Y., Zhang, L., Zhu, X., Gao, J., Huang, W., Zhou, Y., Song, Y., Zhang, Q., and Wang, Y.: Identifying ammonia hotspots in China using a national observation network, *Environ. Sci. Technol.*, 52, 3926–3934, <https://doi.org/10.1021/acs.est.7b05235>, 2018.
- Pandolfi, M., Amato, F., Reche, C., Alastuey, A., Otjes, R. P., Blom, M. J., and Querol, X.: Summer ammonia measurements in a densely populated Mediterranean city, *Atmos. Chem. Phys.*, 12, 7557–7575, <https://doi.org/10.5194/acp-12-7557-2012>, 2012.
- Paulot, F., Jacob, D. J., Pinder, R. W., Bash, J. O., Travis, K., and Henze, D. K.: Ammonia emissions in the United States, European Union, and China derived by high-resolution inversion of ammonium wet deposition data: Interpretation with a new agricultural emissions inventory (MASAGE\_NH3), *J. Geophys. Res.-Atmos.*, 119, 4343–4364, <https://doi.org/10.1002/2013jd021130>, 2014.
- Peng, S., Huang, J., Zhong, X., Yang, J., Wang, G., Zou, Y., Zhang, F., Zhu, Q., Buresh, R., and Witt, C.: Challenge and opportunity in improving fertilizer-nitrogen use efficiency of irrigated rice in China, *Agr. Sci. China*, 1, 776–785, 2002.
- Pinder, R. W., Walker, J. T., Bash, J. O., Cady-Pereira, K. E., Henze, D. K., Luo, M. Z., Osterman, G. B., and Shephard, M. W.: Quantifying spatial and seasonal variability in atmospheric ammonia with in situ and space-based observations, *Geophys. Res. Lett.*, 38, L04802, <https://doi.org/10.1029/2010gl046146>, 2011.
- Shephard, M. W. and Cady-Pereira, K. E.: Cross-track Infrared Sounder (CrIS) satellite observations of tropospheric ammonia, *Atmos. Meas. Tech.*, 8, 1323–1336, <https://doi.org/10.5194/amt-8-1323-2015>, 2015.
- Someya, Y., Imasu, R., Shiomi, K., and Saitoh, N.: Atmospheric ammonia retrieval from the TANSO-FTS/GOSAT ther-

- mal infrared sounder, *Atmos. Meas. Tech.*, 13, 309–321, <https://doi.org/10.5194/amt-13-309-2020>, 2020.
- Van Damme, M., Clarisse, L., Heald, C. L., Hurtmans, D., Ngadi, Y., Clerbaux, C., Dolman, A. J., Erisman, J. W., and Coheur, P. F.: Global distributions, time series and error characterization of atmospheric ammonia (NH<sub>3</sub>) from IASI satellite observations, *Atmos. Chem. Phys.*, 14, 2905–2922, <https://doi.org/10.5194/acp-14-2905-2014>, 2014.
- Van Damme, M., Whitburn, S., Clarisse, L., Clerbaux, C., Hurtmans, D., and Coheur, P.-F.: Version 2 of the IASI NH<sub>3</sub> neural network retrieval algorithm: near-real-time and reanalysed datasets, *Atmos. Meas. Tech.*, 10, 4905–4914, <https://doi.org/10.5194/amt-10-4905-2017>, 2017.
- Van Damme, M., Clarisse, L., Whitburn, S., Hadji-Lazaro, J., Hurtmans, D., Clerbaux, C., and Coheur, P. F.: Industrial and agricultural ammonia point sources exposed, *Nature*, 564, 99–103, <https://doi.org/10.1038/s41586-018-0747-1>, 2018.
- Wang, S., Nan, J., Shi, C., Fu, Q., Gao, S., Wang, D., Cui, H., Saiz-Lopez, A., and Zhou, B.: Atmospheric ammonia and its impacts on regional air quality over the megacity of Shanghai, China, *Sci. Rep.-UK*, 5, 1–13, <https://doi.org/10.1038/srep15842>, 2015.
- Wang, Z., Zhang, X., Liu, L., Cheng, M., and Xu, J.: Spatial and seasonal patterns of atmospheric nitrogen deposition in North China, *Atmospheric and Oceanic Science Letters*, 13, 188–194, <https://doi.org/10.1080/16742834.2019.1701385>, 2020.
- Warner, J. X., Wei, Z., Strow, L. L., Dickerson, R. R., and Nowak, J. B.: The global tropospheric ammonia distribution as seen in the 13-year AIRS measurement record, *Atmos. Chem. Phys.*, 16, 5467–5479, <https://doi.org/10.5194/acp-16-5467-2016>, 2016.
- Werner, M., Kryza, M., Geels, C., Ellermann, T., and Skjøth, C. A.: Ammonia concentrations over Europe – application of the WRF-Chem model supported with dynamic emission, *Pol. J. Environ. Stud.*, 26, 1323–1341, <https://doi.org/10.15244/pjoes/67340>, 2017.
- Wesely, M.: Parameterization of surface resistances to gaseous dry deposition in regional-scale numerical models, *Atmos. Environ.*, 41, 52–63, <https://doi.org/10.1016/j.atmosenv.2007.10.058>, 2007.
- Whitburn, S., Van Damme, M., Clarisse, L., Bauduin, S., Heald, C., Hadji-Lazaro, J., Hurtmans, D., Zondlo, M. A., Clerbaux, C., and Coheur, P. F.: A flexible and robust neural network IASI-NH<sub>3</sub> retrieval algorithm, *J. Geophys. Res.-Atmos.*, 121, 6581–6599, <https://doi.org/10.1002/2016JD024828>, 2016.
- Xu, W., Luo, X. S., Pan, Y. P., Zhang, L., Tang, A. H., Shen, J. L., Zhang, Y., Li, K. H., Wu, Q. H., Yang, D. W., Zhang, Y. Y., Xue, J., Li, W. Q., Li, Q. Q., Tang, L., Lu, S. H., Liang, T., Tong, Y. A., Liu, P., Zhang, Q., Xiong, Z. Q., Shi, X. J., Wu, L. H., Shi, W. Q., Tian, K., Zhong, X. H., Shi, K., Tang, Q. Y., Zhang, L. J., Huang, J. L., He, C. E., Kuang, F. H., Zhu, B., Liu, H., Jin, X., Xin, Y. J., Shi, X. K., Du, E. Z., Dore, A. J., Tang, S., Collett Jr., J. L., Goulding, K., Sun, Y. X., Ren, J., Zhang, F. S., and Liu, X. J.: Quantifying atmospheric nitrogen deposition through a nationwide monitoring network across China, *Atmos. Chem. Phys.*, 15, 12345–12360, <https://doi.org/10.5194/acp-15-12345-2015>, 2015.
- Zhang, L., Chen, Y., Zhao, Y., Henze, D. K., Zhu, L., Song, Y., Paulot, F., Liu, X., Pan, Y., Lin, Y., and Huang, B.: Agricultural ammonia emissions in China: reconciling bottom-up and top-down estimates, *Atmos. Chem. Phys.*, 18, 339–355, <https://doi.org/10.5194/acp-18-339-2018>, 2018.
- Zhang, Q., Yu, Y., Zhang, W., Luo, T., and Wang, X.: Cloud detection from FY-4A's geostationary interferometric infrared sounder using machine learning approaches, *Remote Sens.*, 11, 3035, <https://doi.org/10.3390/rs11243035>, 2019.
- Zhang, X., Wu, Y., Liu, X., Reis, S., Jin, J., Dragosits, U., Van Damme, M., Clarisse, L., Whitburn, S., Coheur, P.-F. O., and Gu, B.: Ammonia emissions may be substantially underestimated in China, *Environ. Sci. Technol.*, 51, 12089–12096, <https://doi.org/10.1021/acs.est.7b02171>, 2017.
- Zhang, X. M., Ren, C. C., Gu, B. J., and Chen, D. L.: Uncertainty of nitrogen budget in China, *Environ. Pollut.*, 286, 117216, <https://doi.org/10.1016/j.envpol.2021.117216>, 2021.
- Zhang, Y., Liu, X., Zhang, F., Ju, X., Zou, G., and Hu, K.: Spatial and temporal variation of atmospheric nitrogen deposition in the North China Plain, *Acta Ecologica Sinica*, 26, 1633–1638, [https://doi.org/10.1016/S1872-2032\(06\)60026-7](https://doi.org/10.1016/S1872-2032(06)60026-7), 2006.
- Zhou, F., Ciais, P., Hayashi, K., Galloway, J., Kim, D.-G., Yang, C., Li, S., Liu, B., Shang, Z., and Gao, S.: Re-estimating NH<sub>3</sub> emissions from Chinese cropland by a new nonlinear model, *Environ. Sci. Technol.*, 50, 564–572, <https://doi.org/10.1021/acs.est.5b03156>, 2016.